ADVANCES IN ATMOSPHERIC SCIENCES, VOL. 30, NO. 6, 2013, 1587–1600

Evaluation of Spring Persistent Rainfall over East Asia in CMIP3/CMIP5 AGCM Simulations

ZHANG Jie[1,2,3] (张洁), Laurent LI [2,3], ZHOU Tianjun*[1] (周天军), and XIN Xiaoge[3] (辛晓歌)

[1]*State Key Laboratory of Numerical Modeling for Atmospheric Sciences and Geophysical Fluid Dynamics, Institute of Atmospheric Physics, Chinese Academy of Sciences, Beijing* 100029

[2]*Laboratoire de Météorologie Dynamique/The Centre National de la Recherche Scientifique, Université Paris 6, France*

[3]*National Climate Center, China Meteorological Administration, Beijing* 100081

(Received 26 June 2012; revised 5 February 2013; accepted 6 February 2013)

ABSTRACT

The progress made from Phase 3 to Phase 5 of the Coupled Model Intercomparison Project (CMIP3 to CMIP5) in simulating spring persistent rainfall (SPR) over East Asia was examined from the outputs of nine atmospheric general circulation models (AGCMs). The majority of the models overestimated the precipitation over the SPR domain, with the mean latitude of the SPR belt shifting to the north. The overestimation was about 1mm d^{-1} in the CMIP3 ensemble, and the northward displacement was about 3°, while in the CMIP5 ensemble the overestimation was suppressed to 0.7 mm d^{-1} and the northward shift decreased to 2.5°. The SPR features a northeast–southwest extended rain belt with a slope of 0.4°N/°E. The CMIP5 ensemble yielded a smaller slope (0.2°N/°E), whereas the CMIP3 ensemble featured an unrealistic zonally-distributed slope. The CMIP5 models also showed better skill in simulating the interannual variability of SPR. Previous studies have suggested that the zonal land–sea thermal contrast and sensible heat flux over the southeastern Tibetan Plateau are important for the existence of SPR. These two thermal factors were captured well in the CMIP5 ensemble, but underestimated in the CMIP3 ensemble. The variability of zonal land–sea thermal contrast is positively correlated with the rainfall amount over the main SPR center, but it was found that an overestimated thermal contrast between East Asia and South China Sea is a common problem in most of the CMIP3 and CMIP5 models. Simulation of the meridional thermal contrast is therefore important for the future improvement of current AGCMs.

Key words: model comparison; CMIP3; CMIP5; spring persistent rainfall (SPR); atmospheric general circulation model (AGCM)

Citation: Zhang, J., L. Li, T. J. Zhou, and X. G. Xin, 2013: Evaluation of spring persistent rainfall over East Asia in CMIP3/CMIP5 atmospheric AGCM simulations. *Adv. Atmos. Sci.*, **30**(6), 1587–1600, doi: 10.1007/s00376-013-2139-7.

1. Introduction

Climate in East Asia is dominated by the monsoon, with abundant rainfall in summer and dry conditions in winter. However, large amounts of rainfall can also be observed in spring (March to May) in East Asia, before the main summer monsoon. Spring Persistent Rainfall (SPR) can contribute >30% of total annual rainfall in Southeast China. As the name suggests, such rainfall events are quite persistent during the whole spring season, and also shows large interannual variability. Extreme SPR anomalies can greatly affect human activities in southeastern China (Hu et al., 2003), and are thus closely monitored by local meteorological services.

Efforts devoted to studying SPR have been increasing in recent years (e.g. Wang et al., 2002; Xin et al., 2011). It is believed that the thermal and dynam-

*Corresponding author: ZHOU Tianjun, zhoutj@lasg.iap.ac.cn

Table 1. Description of the AGCMs used in the study.

Letter code	Name used in the discussion	AGCM	Resolution	Institute	CMIP Phase
A3	cnrm_cm3	-	T42L45	CNRM	CMIP3
A5	CNRM-CM5		TL127L31		CMIP5
B3	giss_model_e_r	-	4.0° (lat) × 5.0° (lon) L20	NASA/GISS	CMIP3
B5	GISS-E2-R		2.0° (lat) × 2.5° (lon) L40		CMIP5
C3	inmcm3_0	-	4.0° (lat) × 5.0° (lon) L21	INM	CMIP3
C5	INMCM4		1.5° (lat) × 2.0° (lon) L21		CMIP5
D3	ipsl_cm4	LMDZ4	2.5° (lat) ×3.75° (lon) L19	IPSL	CMIP3
D5-1	IPSL-CM5A-LR	LMDZ4_v5	96×95×39		CMIP5
D5-2	IPSL-CM5B-LR	LMDZ5_NPv3.1	96×95×39		
E3-1	miroc3_2_hires	MIROC3_2_hires	T106 L56	CCSR	CMIP3
E3-2	miroc3_2_medres	MIROC3_2_medres	T42L20		
E5	MIROC5	MIROC-AGCM6	T85L40		CMIP5
F3	mpi_echam5	ECHAM5	T63 L32	MPI	CMIP3
F5	MPI-ESM-LR	ECHAM6	T63L47		CMIP5
G3	mri_cgcm2_3_2a	-	T42L30	MRI	CMIP3
G5	MRI-CGCM3	GSMUV (gsmuv-110112o)	TL159L48		CMIP5
H3	ncar_ccsm3_0	CAM3	T85L26	NCAR	CMIP3
H5	CCSM4	CAM4	0.94° (lat) × 1.25° (lon) L26		CMIP5

ical effects of the Tibetan Plateau (TP), important in summer, also play roles in the transitional season (Yanai et al., 1992; Ye and Wu, 1998). Tian and Yasunari (1998) advanced the idea that SPR is a consequence of the rapid increase of land–sea thermal contrast between the Indochina Peninsula and the western North Pacific. The southerlies associated with the eastward temperature gradient are important for moisture transport to Central China and moisture convergence. The close relationship is evident at both seasonal and interannual time scales. Wan and Wu (2007) further argued that the climatic behavior of SPR is the result of dynamical forcing and thermal forcing of the TP. Numerical sensitivity experiments showed that SPR would disappear without the influence of the TP, and the southwesterly along the southeastern flank of the TP would increase almost linearly with the amount of total diabatic heating with TP rising.

Climate simulations performed under the framework of the Fourth Assessment Report of the Intergovernmental Panel on Climate Change (IPCC, 2007) and the recent Fifth Assessment Report (IPCC, 2013)[a] provide a unique opportunity to understand rainfall in East Asia. The region is a hot-spot for climate studies, and thus the assessment of model skill is a very important topic for future climate projections, with a few studies having already been published in this regard with respect to the summer season (e.g. Li and Zhang, 2009; Li et al., 2009; Zhou et al., 2009; Chen et al., 2010; Zhou and Zou, 2010; Zou et al., 2010; Sperber et al., 2012). In the present study, we wanted to extend the diagnostics to spring, with a focus on SPR. The main objective was to evaluate the abilities of current state-of-the-art AGCMs in capturing the behavior of SPR relative to previous model generations, and discuss possible factors contributing to misrepresentations in current Phase 5 of the Coupled Model Intercomparison Project (CMIP5) AGCMs.

The remainder of the paper is organized as follows. The models and datasets used in the study are described in section 2. In section 3, we evaluate the performance of the chosen AGCMs in reproducing SPR climatology over East Asia in terms of mean precipitation, mean circulation associated with SPR, and interannual variability. To close, a discussion and summary are provided in section 4.

2. Models and data

The model datasets used in the study were AMIP (Atmospheric Model Intercomparison Project) simulations from nine AGCMs developed in eight groups (some groups contributed more than one model), as an integral part of CMIP3/CMIP5. Each simulation was forced by identically prescribed historical ocean and sea ice boundary conditions (Rayner et al., 2003; Taylor et al., 2012). A brief summary of these models is shown in Table 1. General descriptions of the models with references are available from the following websites: http://www-pcmdi.llnl.gov/projects/modeldoc/amip2/ and http://cmip-pcmdi.llnl.gov/cmip5/availability.html). In this study,

[a]IPCC, 2013: *Climate change 2013: The physical science basis. Contribution of Working Group I to the Fifth Assessment Report of the Intergovernmental Panel on Climate Change*. Underway.

we used a dataset covering 1980–97, a common period for all models.

The CPC Merged Analysis of Precipitation (CMAP; Xie and Arkin, 1997) dataset, covering the same period, was employed to evaluate the SPR simulations. Atmospheric circulations from the ERA40 reanalysis data were also used for the purpose of model assessment (Uppala et al., 2005). The physical variables used in the study included monthly specific humidity and meridional and zonal wind components at eight standard levels; namely, 1000, 925, 850, 700, 600, 500, 400 and 300 hPa. Surface sensible heat flux (SH) and air temperature at 850 hPa were also used for the investigation. The horizontal resolution for both the CMAP precipitation data and ERA40 reanalysis is 2.5° × 2.5°.

To facilitate the comparison, all the CMIP3/CMIP5 datasets were re-gridded to 2.5°×2.5°. All spatial averaging and correlation calculations used area weighting, where areas changing between meridians at varying latitudes were considered by using the cosine of the latitude as the weights.

3. SPR climatology over East Asia in the AGCMs

3.1 *Mean precipitation*

In this section, the spatial distributions of 18-yr mean precipitation averaged for March–April–May (MAM) from the AGCMs are evaluated against CMAP for the period 1980–97. CMAP is a gridded analysis of global precipitation using gauge observations, satellite estimates, and numerical model predictions. Results from CMAP show great resemblance to the 160-station rainfall climatology compiled by the China Meteorological Administration (data not shown).

Although the time period for our study (MAM) was slightly different from that used by Tian and Yasunari (1998) (from pentad 12 to 26), the spatial structures of precipitation were almost the same. The rainfall in CMAP showed ranges from about 1–7 mm d^{-1} (Fig. 1). The main rain belt extended along the southeastern coastline of China, with a few maximum centers corresponding to regional mountainous areas where rainfall intensity was >7 mm d^{-1}. Diagnostics and numerical studies have indicated that the topography of the Nanling and Wuyi Mountains has a great impact upon the distribution and intensity of the SPR belt (Wan and Wu, 2009; Wan et al., 2009). The mountains can block and lift cold and warm air, strengthening frontogenesis and rainfall. Accordingly, the axis of the SPR belt was superposed over that of the mountain range. The area average CMAP precipitation climatology was 3.02 mm d^{-1} for the SPR domain (21°–39°N, 101°–123°E) and 5.64 mm d^{-1} for the main rainfall center Region A (21.25°–28.75°N, 111.25°–121.25°E).

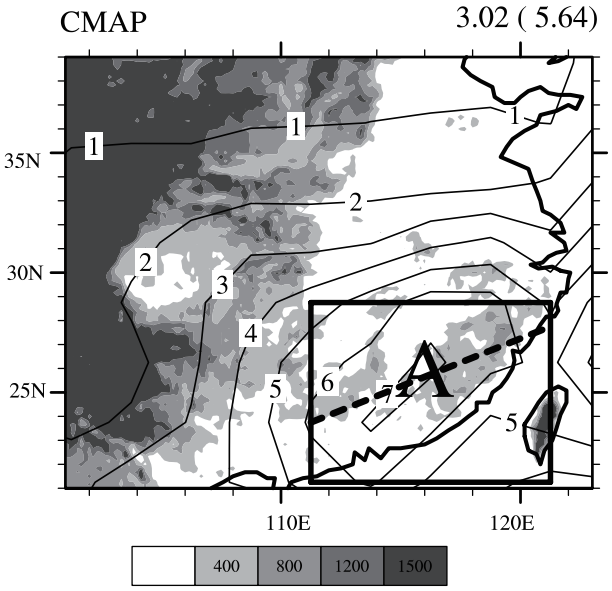

Fig. 1. MAM mean rainfall over East Asia (contours), obtained from CMAP. The contour interval is 1 mm d^{-1}. The regional mean rainfall for the SPR domain (21°–39°N, 101°–123°E) is shown in the top-right corner. The number in parentheses shows the precipitation averaged over the main rainfall center, Region A (21.25°–28.75°N, 111.25°–121.25°E). The shading denotes the topography (units: m). The SPR position based on a linear fit over the longitude range 111.25°–121.25°E to maximum precipitation is shown by the thick dashed line.

To evaluate the simulation of SPR in the AGCMs, it was necessary to give some objective definitions that were able to capture the most important features of SPR, such as the rainfall magnitude as well as the orientation and position of the SPR belt. The location of SPR can be defined as the line of maximum precipitation in the SPR center. In this study, we firstly identified the latitude of maximum precipitation at each longitude point over Region A, and then located SPR by a linear fit to the maximum precipitation. The orientation and position of the SPR belt could then be presented by the slope and mean latitude of the regression line. The linear fit for CMAP is shown by the thick dashed line in Fig. 1. It has a northeast–southwest slope of 0.4°N/°E and mean latitude of 25.75°N. The linear fit of the SPR belt is referred as the SPR line hereafter.

Considering the different spatial resolutions of the atmospheric GCMs, model outputs were interpolated to the CMAP grid (2.5°× 2.5°). Figure 2 shows the climatology maps of SPR in the CMIP3 and CMIP5

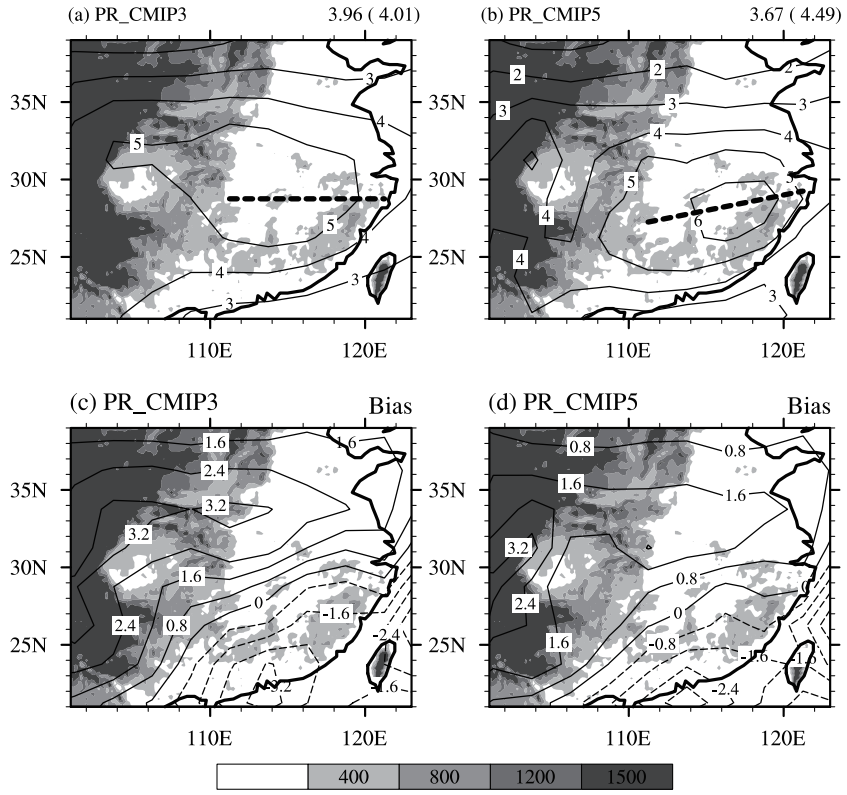

Fig. 2. (a) Multi-model ensemble mean of precipitation simulated by the nine chosen AGCMs that participated in CMIP3 and (b) the corresponding result by their updated versions that participated in CMIP5; (c) and (d) are the model mean biases compared with CMAP. The regional mean precipitation over the SPR domain and the main rainfall center are shown in the top-right corner of (a) and (b). Black dashed lines in (a) and (b) denote the linear regression curves upon the maximum precipitation, as in Fig. 1.

multi-model ensembles and their differences relative to CMAP. In the ensembles, the main rain belt was located over the middle and lower reaches of the Yangtze River valley. That is, precipitation was overestimated over northern China, but underestimated over southern China.

Other differences could also be seen between observations and simulations. Firstly, in the CMIP3 ensemble, the amount of precipitation was 0.94 mm d^{-1} stronger than observed over the SPR domain, but underestimated by about 1.63 mm d^{-1} over the SPR center (Region A). Therefore, the models tend to underestimate the spatial range of the precipitation variation. Secondly, the main rain belt shifted to about 3° north to its normal position (28.75° N). As described by the latitudinal distribution of SPR (Fig. 3) (zonal averaged precipitation over the range 110°–120°E), the maximum rainfall was found to occur at around 26°N in CMAP, but the model ensemble mean peaked north of this latitude, and the peak precipitation amount was underestimated. Spatially, precipitation was deficient in southern China but sufficient over the central and

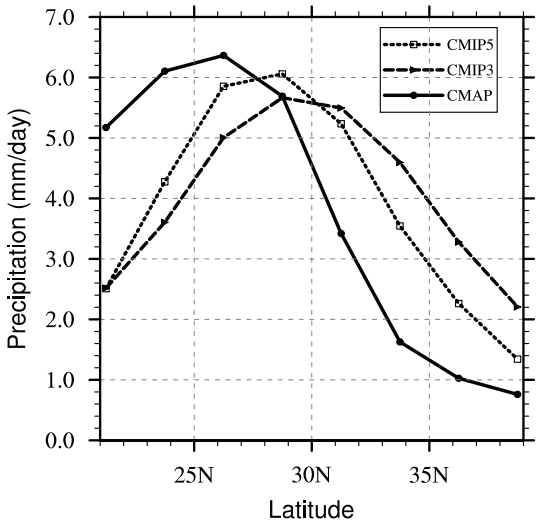

Fig. 3. Zonal averaged MAM precipitation (110°–120°E) from CMAP (black line), ensemble means of the nine CMIP3 models (dashed line), and the CMIP5 models (dotted line).

northern part of the SPR domain. The rainfall bias also led to an unrealistic zonally distributed slope of the SPR belt. Also apparent was spurious rainfall amounts adjacent to the TP, over the northern part of the Sichuan Basin (30°–34°N, 105°–110°E), which seems to be a common problem in both global and regional climate simulations (e.g. Yu et al., 2000; Xue et al., 2004; Wan and Wu, 2007; Chen et al., 2010). The largest disagreement among the AGCMs in this study also occurred in the northeastern part of the Sichuan Basin (Figs. 4 and 5), implying a generally poor performance of the models in reproducing precipitation over this region.

The ensemble behavior of CMIP5 showed substantial improvements relative to CMIP3. The general overestimation of the amount of precipitation was suppressed, decreasing from 3.96 mm d^{-1} in CMIP3 to 3.67 mm d^{-1} in CMIP5, while the rainfall magnitude over Region A increased to 4.49 mm d^{-1}. The location of the SPR belt was also more realistic, such as its northeast–southwest tilted SPR belt with a slope of 0.2°N/°E and about 0.5° southward displacement of the SPR mean latitude relative to that in the CMIP3 ensemble. As shown by the latitudinal distribution of SPR (Fig. 3), the peak rainfall amount and spatial variability of SPR depicted by CMIP5 models were more reasonable than in the CMIP3 models.

We now examine the spatial distribution of rainfall in individual models. Letter code for each model is described in Table 1. In CMIP3 (Fig. 4), a common bias of all the models, except H3 (ncar_ccsm3_0), was the general overestimation of precipitation over the SPR domain, ranging from 0.2 mm d^{-1} (E3-2: miroc3_2_medres) to 2.1 mm d^{-1} (B3: giss_model_e_r). The precipitation over the main rainfall center was underestimated by more than 0.9 mm d^{-1} in all the models. Although the domain-averaged precipitation amount in ncar_ccsm3_0 was close to the observed value, the spatial precipitation variability was small, ranging from 2 to 4 mm d^{-1}. In the updated ver-

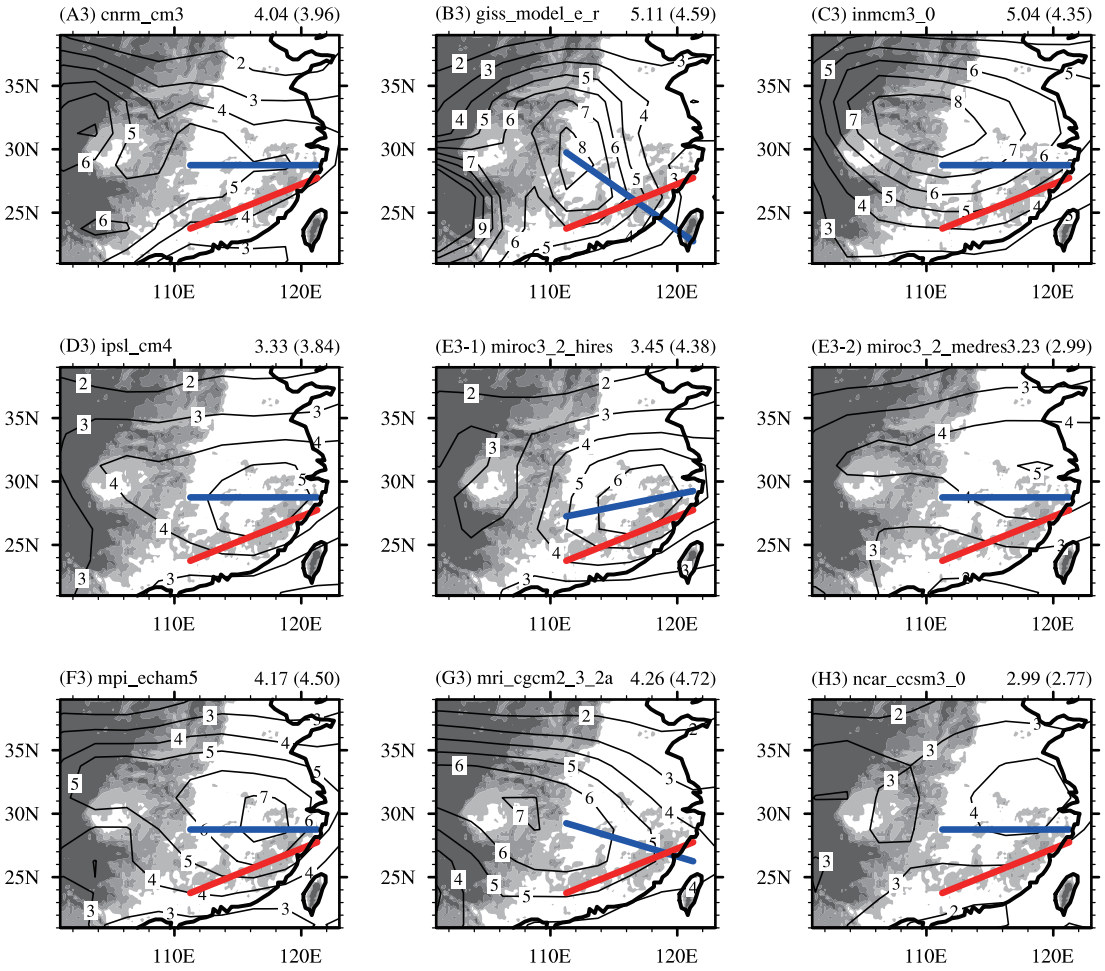

Fig. 4. The same as Fig. 1, but for the results of the CMIP3 models. The SPR line in each CMIP3 model is shown by the blue line. The SPR line in CMAP as a benchmark is shown by the red line.

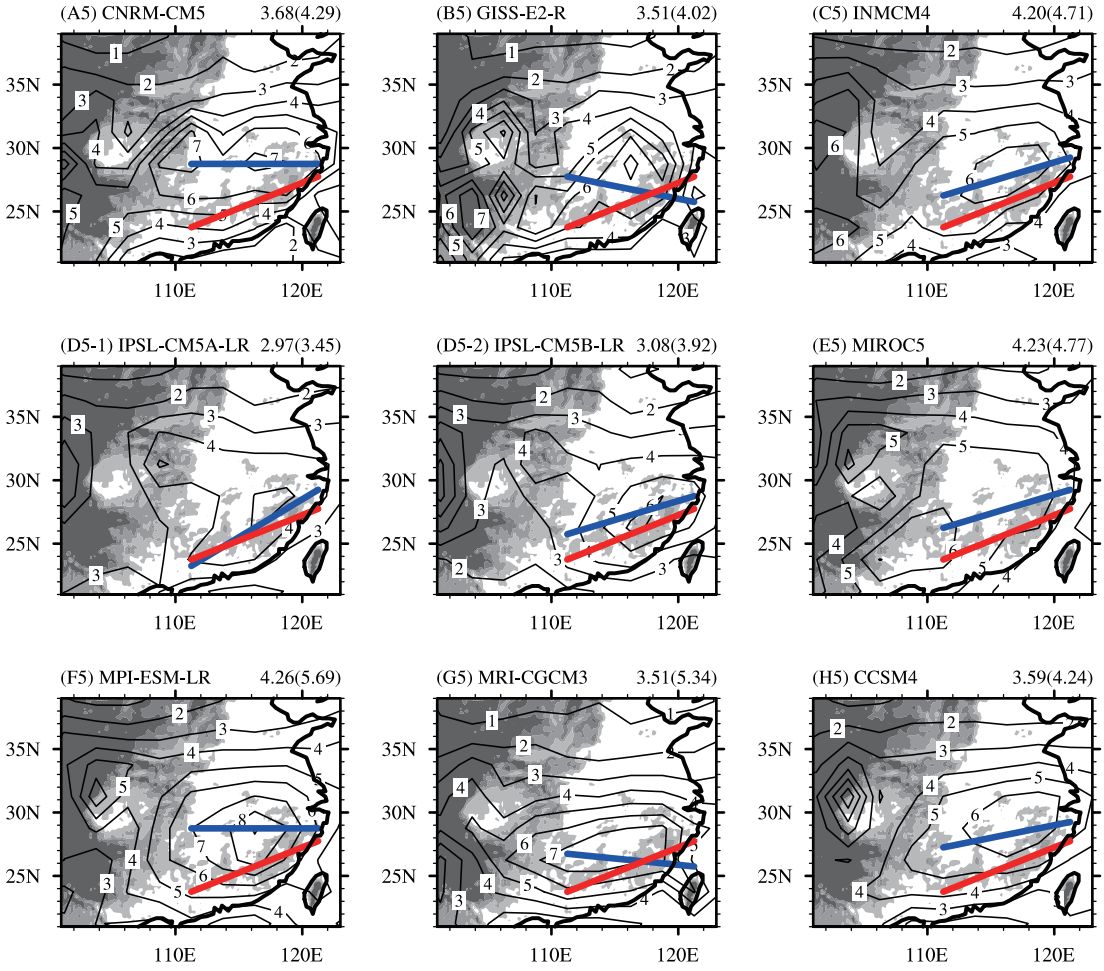

Fig. 5. The same as Fig. 4, but for results of the CMIP5 models.

sions of the models participating in CMIP5 (Fig. 5), the rainfall bias over the SPR domain was smaller, ranging from 0.05 mm d^{-1} (D5-1: IPSL-CM5A-LR) to 1.2 mm d^{-1} (F5: MPI-ESM-LR). The rainfall amount over the main rainfall center was up to 5 mm d^{-1} in F5 (MPI-ESM-LR) and G5 (MRI-CGCM3), close to the CMAP observation.

To facilitate the examination of the location of SPR, the slope and mean latitude of the SPR line are listed in Table 2 and plotted as scatter diagrams in Fig. 6. The average of the nine CMIP5 models yielded a slope and mean latitude closer to CMAP than the CMIP3 ensemble. Five of the CMIP5 models (C5, D5-1, D5-2, E5 and H5), but only one CMIP3 model (E3-1) described a northeast–southwest tilted SPR belt as in CMAP. Six of the nine CMIP3 models (A3, C3, D3, E3-2, F3 and H3) and two of the nine CMIP5 models (A5 and F5) produced a SPR line that was too zonally distributed. B3, B5, G3 and G5 showed unrealistic northwest–southeast tilted rain belts. In terms of mean latitude of the SPR line, although the north-

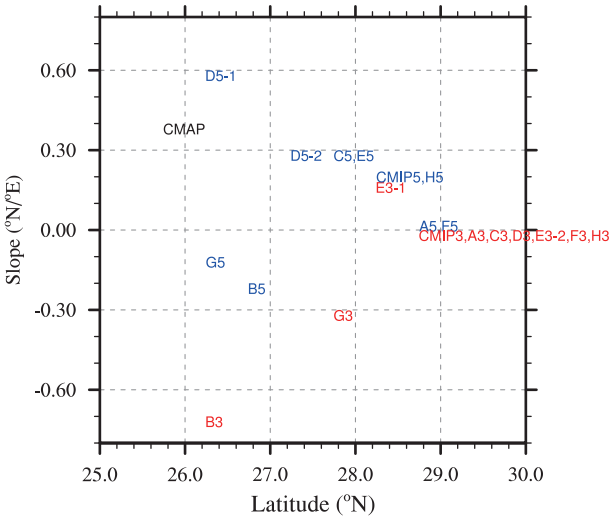

Fig. 6. Mean latitude vs. slope of the SPR line for CMIP3 models (red letters), CMIP5 models (blue letters), and their ensembles. The result for CMAP is also shown (black letters). Model letter codes are given in Table 1.

Table2. Rainfall amounts over the SPR domain and SPR center, slope and mean latitude of the SPR line, zonal and meridional thermal contrasts calculated from CMAP (ERA40), and CMIP3/CMIP5 models and their ensembles. Spatial correlation of SPR between models and CMAP are also shown. Correlation coefficients significant at the 95% level according to the two-tailed Student's *t*-test are shown in bold.

Letter Code	Observation/ model name	Precipitation over SPR domain (mm d^{-1})	Precipitation over SPR center (mm d^{-1})	SPR slope (°N/°E)	SPR mean latitude (°N)	Spatial correlation over SPR domain	East–west thermal contrast [T_{850}(B)−T_{850}(C)]	North–south thermal contrast [T_{850}(E)−T_{850}(F)]
CMAP	CMAP	3.02	5.64	0.4	25.75		ERA40 =2.61	ERA40 = −6.04
CMIP3	CMIP3	3.96	4.01	0	28.75	0.34	2.14	−4.18
CMIP5	CMIP5	3.67	4.49	0.2	28.25	**0.67**	2.63	−4.00
A3	cnrm_cm3	4.04	3.96	0	28.75	0.25	0.25	−5.52
A5	CNRM-CM5	3.68	4.29	0	28.75	**0.48**	3.07	−4.02
B3	giss_model_e_r	5.11	4.59	−0.7	26.25	0.09	1.10	−3.80
B5	GISS-E2-R	3.51	4.02	−0.2	26.75	**0.49**	2.08	−3.55
C3	inmcm3_0	5.04	4.35	0	28.75	−0.11	3.26	−1.50
C5	INMCM4	4.20	4.71	0.3	27.75	**0.50**	1.10	−3.79
D3	ipsl_cm4	3.33	3.84	0	28.75	**0.61**	1.37	−8.52
D5-1	IPSL-CM5A-LR	2.97	3.45	0.6	26.25	**0.55**	2.03	−4.29
D5-2	IPSL-CM5B-LR	3.08	3.92	0.3	27.25	**0.50**	2.64	−4.39
E3-1	miroc3_2_hires	3.45	4.38	0.2	28.25	**0.68**	2.90	−2.89
E3-2	miroc3_2_medres	3.23	2.99	0	28.75	0.10	2.49	−2.36
E5	MIROC5	4.23	4.77	0.3	27.75	**0.60**	3.72	−2.44
F3	mpi_echam5	4.17	4.50	0	28.75	0.37	3.66	−3.28
F5	MPI-ESM-LR	4.26	5.69	0	28.75	**0.67**	4.23	−4.03
G3	mri_cgcm2_3_2a	4.26	4.72	−0.3	27.75	0.44	2.50	−4.81
G5	MRI-CGCM3	3.51	5.34	−0.1	26.25	**0.80**	2.45	−5.52
H3	ncar_ccsm3_0	2.99	2.77	0	28.75	0.01	1.41	−4.97
H5	CCSM4	3.59	4.24	0.2	28.25	**0.54**	2.26	−3.99

ward shift of the SPR belt was also evident for all the CMIP5 models, the SPR belt in the CMIP5 ensemble was located about 0.5° south of that in the CMIP3 ensemble. Model capability in simulating the location of SPR was substantially improved for models developed at INM (C3 vs. C5), IPSL (D3 vs. D5-1 & D5-2), CCSR (E3-1 & E3-2 vs. E5), MRI (G3 vs. G5) and NCAR (H3 vs. H5). The model D5-1 (IPSL-CM5A-LR) was the best in terms of reproducing the distribution of SPR.

In Fig. 7, spatial statistics of rainfall simulation are further evaluated using "Taylor diagrams" (Taylor 2001). The Taylor diagram verifies the relative spatial amplitude ratio to the observation (the radial distance), the cosine spatial correlation between each AGCM and the observation (the angular distance to the x-axis) and the normalized root-mean-square differences (the semicircle with its center at the reference point marked "CMAP"; RMS hereafter). The results

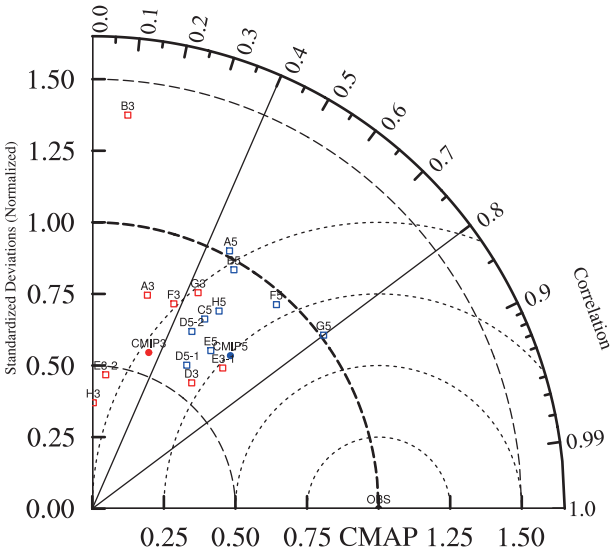

Fig. 7. Taylor diagram for the spatial distribution over the SPR domain obtained from CMAP (black dot), ensemble means of the CMIP3 models (red dot), CMIP5 models (blue dot), and each of the nine chosen AGCMs that participated in CMIP3 (red squares) and their updated versions that participated in CMIP5 (blue squares) in the SPR domain (21°–39°N, 101°–123°E). The result of C3 (inmcm3_0) is not shown because of its negative spatial correlation coefficient with CMAP. The radial distance from the origin denotes the factor between the spatial standard deviation of each dataset and the observation (CMAP). The angular distance from the x-axis denotes the spatial correlation coefficient between each dataset and the observation. That is, the distance between each simulation and the observation quantifies how closely the model's simulated rainfall pattern matches the observation.

for each AGCM dataset as well as the CMIP3/CMIP5 ensembles were examined. The standardized spatial variability along the radial line shows the range between the 37th and 138th percentile values of the amplitude ratio. The AGCMs with spatial standard deviations close to the observation (amplitude ratio equal to 1) all came from the CMIP5 group (A5, B5, F5, and G5). Furthermore, all the CMIP5 models were spatially correlated with CMAP at the 95% significance level according to a two-tailed Student's t-test, with G5 (MRI-CGCM3) at the high end. The too-strong spatial deviation in B3 (giss_model_e_r) was due to its exaggerated intensity of the precipitation center. Generally, spatial deviation in the CMIP5 ensemble was closer to CMAP and the corresponding spatial correlation coefficient (0.67) was about 0.3 more than the CMIP3 ensemble (0.34).

The distribution and intensity of SPR are affected by the topography of the Nanling (24°–26°N, 110°–116°E) and Wuyi (25°–28°N, 116°–118°E) Mountains (Wan and Wu, 2009). Horizontal resolution may be a factor in determining the simulated SPR performance in AGCMs because better resolved topography and surface boundary conditions can lead to better results. For instance, in CMIP3, with a coarse resolution [4° (lat) ×5° (lon)], the rainfall pattern in B3 (giss_model_e_r) showed the largest RMS, and the spatial structure of precipitation in C3 (inmcm3_0) was negatively correlated with CMAP (−0.11). Another example was also observed from the results of E3-1 (MIROC3_2_hires) and E3-2 (MIROC3_2_medres), which are, respectively, high-resolution and medium-resolution models developed at the Center for Climate System Research (CCSR), Tokyo University, Japan (Hasumi and Emori, 2004). Magnitudes of the statistics for the spatial amplitude ratio, spatial correlation and RMS generally agreed better with observation in MIROC3_2_hires. The majority of AGCMs in CMIP5 have a finer resolution relative to previous model generations. The more sophisticated atmospheric physics and dynamics may also contribute to the better model performances of these models.

3.2 *Mean circulation associated with SPR*

The northward displacement of the SPR main rain belt found in the CMIP3/CMIP5 simulations implied a possible shift in the SPR-related mean circulation. The wind pattern based on the ERA40 reanalysis during MAM is shown in Fig. 8a. The main component of the well-developed SPR circulation is the southwesterly across the southern part of East Asia, on the eastern periphery of the TP. This broad-scale feature was captured well by the model ensembles. However, an overdevelopment of the southwesterly over the Yangtze

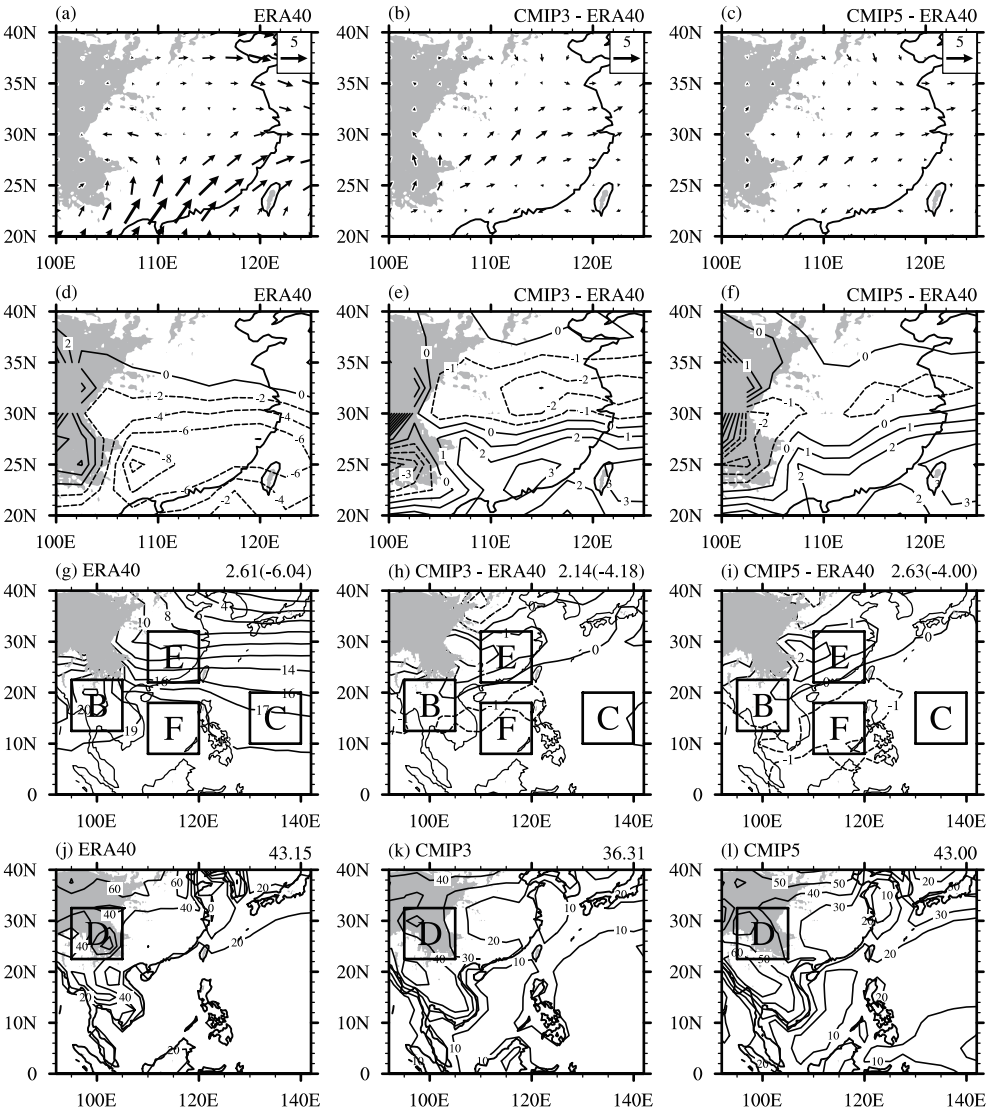

Fig. 8. Climatological spring mean (a) horizontal wind at 850 hPa (units: m s^{-1}), (d) vertically integrated moisture flux divergence (units: mm d^{-1}), (g) temperature at 850 hPa (units: °C), and (j) surface SH (W m^{-2}) in the ERA40 reanalysis. CMIP3 (b, e, h) and CMIP5 (c, f, i) ensemble-mean biases related to the ERA40 reanalysis; (k) and (l) are the ensemble means for surface SH. The numbers in parentheses on the top-right corner of (g, h, i) represent the temperature difference between Region B (12.5°–22.5°N, 95°–105°E) and C (10°–20°N, 130°–140°E), and between Region E (22°–32°N, 110°–120°E) and F (8°–18°N, 110°–120°E). The number shown in the top-right corner of (j, k, l) represents the surface SH in Region D (22.5°–32.5°N, 95°–105°E).

River valley and an underdevelopment across the south coast were also evident (Figs. 8b and c). In comparison with the CMIP3 ensemble, the southwesterly bias was smaller in the CMIP5 ensemble.

East Asia is controlled by strong southwesterly wind during the SPR period and water vapor convergence occurs in front of the center of the southwesterly. The spring moisture flux over East Asia derived from the reanalysis is shown in Fig. 8d. Since atmospheric moisture is concentrated mainly in the lower troposphere (Zhou and Yu, 2005; Zhang et al., 2009), the moisture flux discussed in this study is vertically integrated moisture flux from the surface pressure level to 300 hPa based on monthly mean data. The overdeveloped southwesterly flow over the Yangtze River valley supported a moisture convergence shift to the north. As demonstrated in Figs. 8e–f, the anomalous moisture flux showed an overestimation along the Yangtze

River valley and an underestimation to its south, consistent with the errors in the precipitation climatology. Biases were slightly smaller in the CMIP5 ensemble compared with the CMIP3 ensemble.

The zonal land–sea thermal contrast, which causes the prevailing southerlies over southern China, is an essential factor in SPR formation (Tian and Yasunari, 1998). Figure 8g shows the 850-hPa temperature distribution in ERA40. The temperature maximum is over the western part of the Indochina Peninsula (Region B). The contour over the western Pacific is mostly zonally distributed. In Region C, there is a small zonal temperature gradient to its north and a large zonal temperature gradient to its west. In Tian and Yasunari (1998), the zonal land–sea thermal contrast was defined as the temperature differences between Region B and Region C, and we used this definition to measure the zonal land–sea thermal contrast in the reanalysis and simulations. The zonal thermal contrast was found to be 2.61°C in ERA40 and 2.63°C in the CMIP5 ensemble, but was underestimated by about 0.5°C in the CMIP3 ensemble (2.14°C). The small zonal thermal gradient in the CMIP3 ensemble was due to underestimation in Region B.

Besides the zonal thermal contrast, the SH center over the southeastern TP may also contribute to the existence of SPR, as determined by observational diagnosis (Wan and Wu, 2007). The relationship between the sensible heating and the southwesterly wind over its eastern periphery can be explained with a simplified vorticity equation. As argued in Liu et al. (2004), in the subtropics, vorticity advection and transient processes are weak compared with diabatic heating. The vorticity equation can be simplified into the form of the Sverdrup balance [$\beta v \approx \theta_z^{-1}(f+\zeta)Q_z$, $\theta_z \neq 0$]. In the equation, f is the geostrophic vorticity, β is its meridional gradient, v is meridional wind, θ is potential temperature, ζ is the relative vorticity, Q is diabatic heating and cooling. That is, for the Northern Hemisphere ($f \geqslant 0$), in a statically stable atmosphere ($\theta_z > 0$), a heating that increases with height ($Q_z > 0$) is conducive to poleward flow ($v > 0$). Therefore, in our case, the sensible heating over the southeastern TP can generate a heating profile that increases with altitude and induces the thermally forced lower tropospheric meridional wind at the southeastern flank of the TP, and then affects the formation of SPR.

A spatial examination of SH is shown in Fig. 8j. The maximum SH center can be seen to locate over the southeastern TP (Region D). The regional mean SH was found to be 43.15 W m^{-2}in the ERA40 reanalysis, which was reproduced well in the CMIP5 ensemble (43.0 W m^{-2}), but underestimated by about 7 W m^{-2} in CMIP3.

Generally, better simulated zonal land–sea thermal contrast and SH over the southeastern TP may partly contribute to more reasonable SPR circulation in the CMIP5 ensemble.

3.3 *Interannual variability*

The east–west land–sea thermal contrast may determine the strength of southerly winds as well as the SPR amount. To clarify this, the time series of observed SPR averaged over the main rainfall domain (Region A) is examined in Fig. 9a. The year-to-year changes of the zonal land–sea thermal contrast are shown in Fig. 9b. The SH anomalies were rather weak compared with the magnitude of their climatology. Discrepancies in the interannual variability of SH were found between the ERA40 and National Centers for Atmospheric Prediction/National Center for Atmospheric Research (NCEP/NCAR) reanalysis datasets (Kalnay et al., 1996; data not shown), and therefore we do not show the SH results here.

The interannual characteristics of SPR show no significant trend for the period 1980–97 period. The variability of SPR in the CMIP 5 ensemble was positively correlated with CMAP, with a correlation coefficient

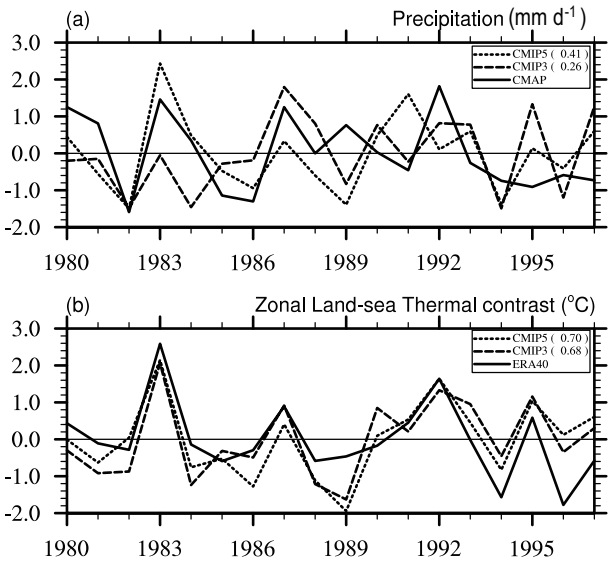

Fig. 9. Interannual variations during 1980–97 of the anomalous (a) precipitation averaged over Region A (units: mm d^{-1}), (b) the thermal contrast between Region B and C (units: °C). The black solid line, dashed line and dotted line represent the results of CMAP (the ERA40 reanalysis) and the CMIP3 and CMIP5 ensemble means, respectively. The numbers in the parentheses in (a) and (b) show the correlation coefficients of the CMIP3 and CMIP5 ensembles with CMAP and ERA40, respectively.

of 0.41. The temporal correlation coefficient was insignificant for the CMIP3 ensemble (0.26). The zonal land–sea thermal contrast was better simulated than rainfall. The multi-model ensembles gave very close estimates to the ERA40 reanalysis, with a correlation coefficient of 0.68 in the CMIP3 ensemble and 0.70 in the CMIP5 ensemble.

As mentioned previously, the zonal land-sea thermal contrast is the basic mechanism of SPR formation. Logically, therefore, one might ask if the zonal temperature gradient between the land and the ocean also plays an important role in SPR variability at the interannual scale? The regional mean precipitation in Region A and land–sea thermal contrast for each MAM period from 1980 to 1997 are shown as scatter plots in Fig. 10. As can be seen, the mean rainfall varies from about 3.6 mm d^{-1} to 6.0 mm d^{-1} in the observation. The CMIP3 ensemble overestimated the range at the low end (about 4.3 mm d^{-1}) but underestimated it at the high end (5.5 mm d^{-1}). The CMIP5 ensemble simulated the amplitude of SPR variability better, although there was also an overestimation of the rainfall amount at the low end. The rainfall amount and zonal thermal contrast were found to show significant inphase variations, with a correlation coefficient of 0.63 in the observation (CMAP vs. ERA40). That is, the amount of precipitation increases when the land–sea thermal contrast is intensified, and vice versa. The positive relationship was reproduced well in both the CMIP3 and CMIP5 ensembles, with correlation coefficients of 0.60 and 0.72, respectively. However, the inphase variations have some exceptions in the CMAP vs. ERA40 reanalysis, such as in 1989, 1990 and years after 1995. Exceptions were also evident in the simulations, such as 1981 and 1982 in CMIP3, and 1982 and 1992 in CMIP5. Therefore, it should be noted that, although the variability of SPR largely follows the variability of zonal land–sea thermal contrast, the zonal thermal contrast is not the only factor responsible for the variability of SPR.

4. Discussion and summary

We evaluated the ability of AGCMs in simulating SPR over East Asia. The simulations of SPR in nine AGCMs that participated in CMIP3 and their updated versions that participated in recent CMIP5 projects were examined. The climatology and interannual variability of SPR were evaluated using the CMAP dataset, and the associated circulation changes and thermal factors were explored.

SPR is a pronounced rainy period before the summer monsoon season in East Asia. Because of the special geographic location with complex topography,

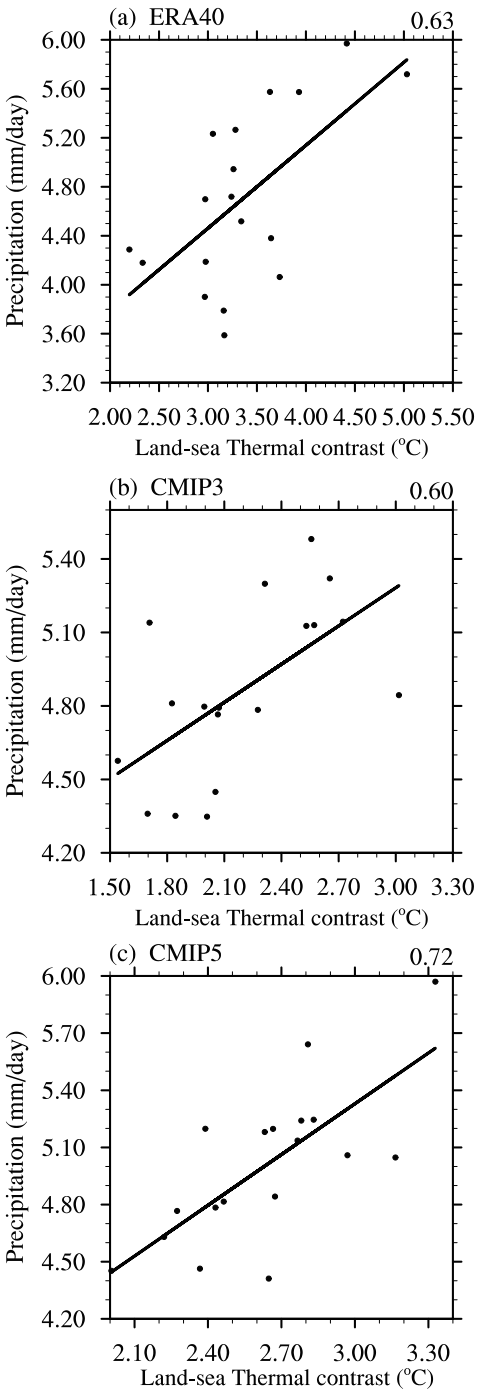

Fig. 10. Scatter plots of regional mean precipitation over Region A (the ordinate; units: mm d^{-1}) vs. temperature difference between Region B and C (the abscissa) of each year from 1980 to 1997. The linear regression lines are shown by the thick black line. (a) Precipitation from CMAP vs. land–sea thermal contrast from ERA40; (b) the CMIP3 ensemble; and (c) the CMIP5 ensemble. The number shown in the top-right corner of each panel is the correlation coefficient between precipitation and zonal land–sea thermal contrast.

SPR reproduction is still a challenge for current state-of-the-art models. In both the CMIP3 and CMIP5 simulations, the AGCMs exaggerated SPR intensity over the SPR domain, but underestimated it in the main SPR center. The simulations showed a northward shift of the main rain belt in comparison with the observation. Furthermore, the orientation of the rain belt was hard to reproduce.

The CMIP5 multi-model ensemble mean outperformed the CMIP3 ensemble in the simulation of the climatological amount of precipitation, as well as the orientation and location of the main rain belt. The CMIP5 ensemble also showed incremental progress in reproducing the interannual variability of SPR.

Investigating the unique phenomenon of SPR in climate models makes it possible to examine model performances and verify the mechanisms identified from observational diagnoses. The zonal land–sea thermal contrast and SH over the southeastern TP, identified from observational diagnoses, are of crucial importance in SPR formulation. These two thermal factors in the CMIP5 ensemble were better reproduced than in the CMIP3 ensemble. A remarkable correspondence between zonal land–sea thermal contrast and rainfall amount during the SPR period was found in the reanalysis, and in the CMIP3/CMIP5 ensembles.

However, a northward shift of the main rain belt was still evident in the CMIP5 models. As shown in Figs. 8h and i, the major biases in the 850-hPa temperature were warming anomalies over East Asia (Region E) and cooling anomalies over the South China Sea (Region F). The north–south thermal contrast was overestimated by about 1.86°C in CMIP3 and 2.04°C in CMIP5. The warming over the East Asian continent and cooling over South China Sea increase the southward thermal contrast, which favors the development of southerly winds. The intensified southerly winds transport excessive water vapor northward and favor a northward migration of the main rain belt. For individual models (Fig. 11), those belonging to CMIP3 showed a larger spread in reproducing both the zonal and meridional thermal contrast as compared to the CMIP5 models. Furthermore, all the CMIP3 and CMIP5 models, except D3, overestimated the meridional thermal contrast. This overestimation may be partly responsible for the misrepresentation of the mean SPR position in CMIP3 and CMIP5 models.

The overestimated north–south thermal contrast was also visible in the other seasons. Figure 12 presents the annual cycle of thermal contrast between East Asia (Region E) and the South China Sea (Region F). Almost all the models tended to overestimate the meridional thermal contrast all the year round, with the overestimation being more pronounced during the first half of the year. The overestimation was about 1.5°C in February, grew to about 2.5°C in March, and sustained until the early summer. As shown in previous works, the northward displacement of the main rain belt is also evident during summertime (e.g. Zou

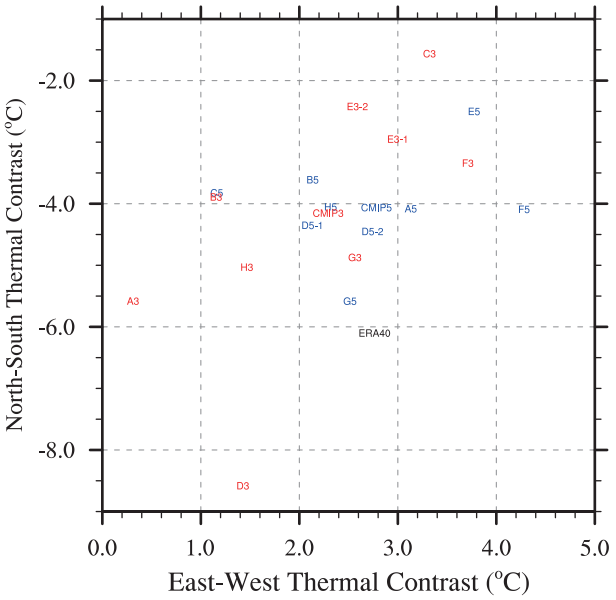

Fig. 11. Zonal thermal contrast (abscissa) vs. meridional thermal contrast (ordinate) for CMIP3 models (red letters), CMIP5 models (blue letters), and their ensembles. The result for ERA40 is also shown (black letter). The zonal thermal contrast is defined as the 850-hPa temperature differences between Region B and C. The meridional thermal contrast is defined as the 850-hPa temperature differences between Region E and F.

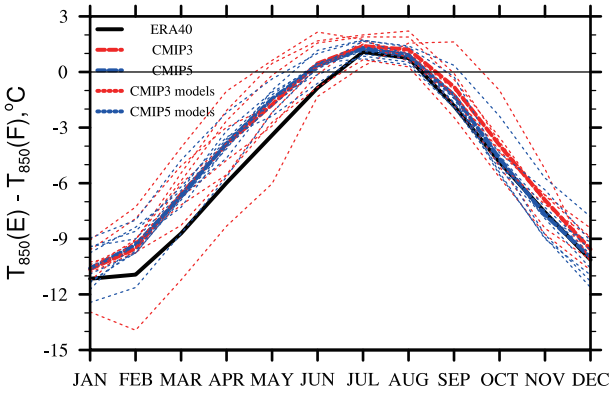

Fig. 12. The annual cycle of 850-hPa temperature difference between Region E and F for the ERA40 reanalysis (black solid line), the CMIP3 models (red dotted lines) and their ensemble (red dashed line), and the CMIP5 models (blue dotted lines) and their ensemble (blue dashed line).

et al., 2010). The overestimated north–south thermal contrast in both the CMIP3 and CMIP5 models could amplify the southerly winds, intensify the moisture transport towards East Asia, and generate more rainfall there.

The weakness of the CMIP3 and CMIP5 models in capturing the meridional thermal contrast at least partly contributes to the northward shift of the main rain belt. Therefore, the ability to capture the meridional thermal contrast is essential for further improving the ability to reproduce SPR, as well as simulate rainfall over East Asia in other seasons.

Acknowledgements. The authors would like to thank the anonymous reviewers for their valuable comments and suggestions to improve the quality of the paper. This work was jointly supported by the Major State Basic Research Development Program of China (973 Program) under Grant No. 2010CB951903, the National Natural Science Foundation of China under grant Nos. 41205043, 41105054 and 40890054 and China Meteorological Administration (GYHY201306062).

REFERENCES

Chen, H., T. Zhou, R. B. Neale, X. Wu, and G. J. Zhang, 2010: Performance of the new NCAR CAM3. 5 in East Asian summer monsoon simulations: Sensitivity to modifications of the convection scheme. *J. Climate,* **23**(13), 3657–3675, doi: 10.1175/2010JCLI3022.1.

Hasumi, H., and S. Emori, 2004: K-1 coupled model (MIROC) description, K-1 technical report 1. Tech. Report, CCSR, The University of Tokyo, 34pp.

Hu, Z. Z., S. Yang, and R. Wu, 2003: Long-term climate variations in China and global warming signals. *J. Geophys. Res.,* **108**(D19), 4614, doi: 10.1029/2003JD003651.

IPCC, 2007: *Climate Change 2007: The Physical Science Basis. Contribution of Working Group I to the Fourth Assessment Report of the Intergovernmental Panel on Climate Change*, Solomon et al., Eds., Cambridge University Press, Cambridge, United Kingdom and New York, NY, USA, 1009pp.

Kalnay, E., and Coauthors, 1996: The NCEP/NCAR 40-year reanalysis project. *Bull. Amer. Meteor. Soc.,* **77**, 437–471.

Li, J., and L. Zhang, 2009: Wind onset and withdrawal of Asian summer monsoon and their simulated performance in AMIP models. *Climate Dyn.,* **32**, 935–968, doi: 10.1007/s00382-008-0465-8.

Li, J., Y. Liu, and G. Wu, 2009: Cloud radiative forcing in Asian monsoon region simulated by IPCC AR4 AMIP models. *Adv. Atmos. Sci.,* **26**(5), 923–939, doi: 10.1007/s00376-009-8111-x.

Liu, Y., G. Wu, and R. Ren, 2004: Relationship between the subtropical anticyclone and diabatic heating. *J. Climate,* **17**(4), 682–698.

Rayner, N., D. Parker, E. Horton, C. Folland, L. Alexander, D. Rowell, E. Kent, and A. Kaplan, 2003: Global analyses of sea surface temperature, sea ice, and night marine air temperature since the late nineteenth century. *J. Geophys. Res.,* **108**(D14), 4407, doi: 10.1029/2002JD002670.

Sperber, K. R., H. Annamalai, I.-S. Kang, A. Kitoh, A. Moise, A. Turner, B. Wang and T. Zhou, 2012: The Asian summer monsoon: an intercomparison of CMIP5 vs. CMIP3 simulations of the late 20th century. *Climate Dyn.*, 1–34, doi: 10.1007/s00382-012-1607-6.

Taylor, K. E., 2001: Summarizing multiple aspects of model performance in a single diagram. *J. Geophys. Res.,* **106**(D7), 7183-7192, doi: 10.1029/2000JD 900719.

Taylor, K. E., R. J. Stouffer, and G. A. Meehl, 2012: An overview of CMIP5 and the experiment design. *Bull. Amer. Meteor. Soc.*, **93**, 485–498, doi: http://dx.doi.org/10.1175/BAMS-D-11-00094.1.

Tian, S. F., and T. Yasunari, 1998: Climatological aspects and mechanism of spring persistent rains over central China. *J. Meteor. Soc. Japan,* **76**, 57–71.

Uppala, S. M., and Coauthors, 2005: The ERA40 reanalysis. *Quart. J. Roy. Meteor. Soc.,* **131**(612), 2961–3012, doi: 10.1256/qj.04.176.

Wan, R. J., and G. X. Wu, 2007: Mechanism of the spring persistent rains over southeastern China. *Science in China* (*D*), **50**(1), 130–144, doi: 10.1007/s11430-007-2069-2.

Wan, R. J., and G. X. Wu, 2009: Temporal and spatial distributions of the spring persistent rains over southeastern China. *Acta Meterologica Sinica*, **23** (5), 598–608. (in Chinese)

Wan, R. J., B. K. Zhao, and G. X. Wu, 2009: New evidences on the climatic causes of the formation of the spring persistent rains over southeastern China. *Adv. Atmos. Sci.*, **26**(6), 1081–1087, doi: 10.1007/s00376-009-7202-z.

Wang, H. J., F. Xue, and G. Q. Zhou, 2002: The spring monsoon in south china and its relationship to Large-Scale circulation features. *Adv. Atmos. Sci.,* **19**(4), 651–664, doi: 10.1007/s00376-002-0005-0.

Xie, P., and P. A. Arkin, 1997: Global precipitation: A 17-year monthly analysis based on gauge observations, satellite estimates, and numerical model outputs. *Bull. Amer. Meteor. Soc.*, **78,** 2539–2558.

Xin, X. G., T. J. Zhou, and Z. X. Li, 2011: Regional climate simulation over eastern China in spring by a variable resolution AGCM. *Acta Meteorologica Sinica,* **69**(4), 682–692. (in Chinese)

Xue, Y., H. Juang, W. Li, S. Prince, R. DeFries, Y. Jiao, and R. Vasic, 2004: Role of land surface processes in monsoon development: East Asia and West Africa. *J. Geophys. Res.,* **109**, D03105, doi: 10.1029/2003JD003556.

Yanai, M., C. Li, and Z. Song, 1992: Seasonal heating of the Tibetan Plateau and its effects on the evolu-

tion of the Asian summer monsoon. *J. Meteor. Soc. Japan,* **70**(1), 319–350.

Ye, D. Z., and G. X. Wu, 1998: The role of the heat source of the Tibetan Plateau in the general circulation. *Meteor. Atmos. Phys.,* **67**(1), 181–198.

Yu, R. C., W. Li, X. H. Zhang, Y. M. Liu, Y. Q. Yu, H. L. Liu, and T. J. Zhou, 2000: Climatic features related to eastern China summer rainfalls in the NCAR CCM3. *Adv. Atmos. Sci.,* **17**(4), 503–518, doi: 10.1007/s00376-000-0014-9.

Zhang, J., T. J. Zhou, R. C. Yu, and X. G. Xin, 2009: Atmospheric water vapor transport and corresponding typical anomalous spring rainfall patterns in China. *Chinese J. Atmos. Sci.,* **33**(1), 121–134. (in Chinese)

Zhou, T. J., and R. C. Yu, 2005: Atmospheric water vapor transport associated with typical anomalous summer rainfall patterns in China. *J. Geophys. Res.,* **110**, D08104, doi: 10.1029/2004JD005413.

Zhou, T., and L. Zou, 2010: Understanding the predictability of East Asian summer monsoon from the reproduction of land-sea thermal contrast change in AMIP-type simulation. *J. Climate,* **23**(22), 6009–6026, doi: 10.1175/2010JCLI3546.1.

Zhou, T., B. Wu, and B. Wang, 2009: How well do atmospheric general circulation models capture the leading modes of the interannual variability of the Asian-Australian monsoon? *J. Climate,* **22**(5), 1159–1173, doi: 10.1175/2008JCLI2245.1.

Zou, L., T. Zhou, L. Z.-X. Li, J. Zhang, 2010: East China summer rainfall variability of 1958–2000: Dynamical downscaling with a variable-resolution AGCM. *J. Climate,* **23**, 6394–6408.